Letter Vol. 49, No. 4 / 15 February 2024 / Optics Letters 1097

Optics Letters

Second-harmonic flat-top beam shaping via a three-dimensional nonlinear photonic crystal

Ruonan Wang,[1] Qiang Cao,[1,*] Xiaoliang Wang,[1] Xiaoyu Tian,[2] and Fengchang Li[1]

[1] The Institute of Technological Sciences, Wuhan University, Wuhan 430072, China
[2] School of Mechanical Engineering, Wuhan Polytechnic University, Wuhan 430048, China
*caoqiang@whu.edu.cn

Received 21 December 2023; revised 24 January 2024; accepted 25 January 2024; posted 29 January 2024; published 15 February 2024

We experimentally extend the nonlinear Gaussian to flat-top beam shaping from one to two dimensions through a three-dimensional nonlinear photonic crystal. Employing a near-infrared femtosecond laser, we induce a modification inside lithium niobate to achieve a second-order nonlinear optical coefficient modulation in three dimensions. The flat-topped truncation of wavefront has been adjusted in a mutual perpendicular coordinate separately. Among the generated flat-topped beams, the optimal flatness is 97.1%, and the nonlinear conversion efficiency is 10^{-2} at the peak power of 37 kW with the interaction length of 630 μm. By adding an extra dimension, our work simultaneously enables full-wavefront flat-top distribution and nonlinear frequency conversion.

https://doi.org/10.1364/OL.516606

The uniform irradiation of a laser is necessary for inertial confinement fusion [1–3], biomedical imaging [4], optical trapping [5], and space debris removal [6]. A flat-top beam with uniform distribution has been extensively studied in linear optics [7,8], while its nonlinear generation has rarely been explored and remains challenging. A nonlinear photonic crystal (NPC) characterizes a spatially varied second-order nonlinear optical coefficient ($\chi^{(2)}$) which converts energy efficiently in a frequency conversion via the quasi-phase matching (QPM) [9,10]. Lithium niobate exhibits exceptional nonlinear, electro-optical, ferroelectric, and thermoelectric characteristics, making it the preferred material for the NPC. Imeshev *et al.* modulated $\chi^{(2)}$ in lithium niobate into laterally inhomogeneous periodic distribution by lithography, which enabled the second-harmonic (SH) beam to be flattened in one dimension [11]. However, in traditional techniques (e.g., electric field poling [12,13] and lithography [14]), the modulations of $\chi^{(2)}$ in the NPC are limited to two dimensions, due to the lack of fabrication technologies capable of three-dimensional (3D) nonlinearity engineering. One of the dimensions has to be used for the frequency conversion of the QPM. Therefore, the 2D flat-top NPC is still unable to achieve full-wavefront shaping with only one dimension left.

A near-infrared femtosecond laser, which can be focused inside a transparent material, is essential for $\chi^{(2)}$ nonlinearity engineering in three dimensions [15–19]. Meanwhile, femtosecond pulses may change $\chi^{(2)}$ values due to material modification, which are permanent and cannot be removed by annealing above the Curie temperature [20]. The 3D NPC fabricated by this technique has been widely applied to laser frequency conversion [21,22], nonlinear beam shaping [23,24,25], and nonlinear holography [26,27].

In this work, we generate the second-harmonic flat-top beam through the 3D conic NPC with a near-infrared femtosecond laser. The femtosecond laser induces a modification of lithium niobate to achieve the modulation of its $\chi^{(2)}$ values. The design principles of the 3D NPC are shown in Fig. 1. The design principles apply only to the conditions of the undepleted-pump approximation. The period length of the QPM grating determines the intensity and efficiency of the second-harmonic generation (SHG). Therefore, a QPM grating structure with the laterally varying period length can be used to convert an ideal uniform SH intensity distribution. In the region without periodicity, the SH conversion efficiency is negligible. The magnitude of truncation factor "a" represents the ratio of the flat-top beam's uniform region radius to the pump beam's waist radius. The truncation factor, which is noted as "a," is the product of its magnitude "a" and the waist radius, with positive and negative values corresponding to the x axis (or z axis) directions from the beam spot's center taken as the origin. The fundamental beam is truncated by the 3D NPC, so that the SH has a flat intensity profile over some range $x\in[-\mathrm{a},\mathrm{a}]$, $z\in[-\mathrm{a},\mathrm{a}]$. For a given pump beam profile, the drive is controlled by the interaction length L. It should be marked that the specific 3D NPC is available only for the given pump beam. Therefore, based on the referenced work in 1998 [11], for a Gaussian fundamental beam, the expansion of the interaction length into a two-dimensional functional form is chosen as

$$L = L_0 \begin{cases} \exp\left(\dfrac{2(x^2-\mathrm{a}^2)}{\omega_x^2}\right)\exp\left(\dfrac{2(z^2-\mathrm{a}^2)}{\omega_z^2}\right) & |x|\le \mathrm{a},\ |z|\le \mathrm{a} \\ 1 & |x|>\mathrm{a},\ |z|>\mathrm{a} \end{cases}, \tag{1}$$

where L_0 is the length of the QPM grating and ω_x and ω_z are the 1/e electric field radius of the Gaussian pump beam on the x and z directions, respectively.

The incident fundamental beam propagates along the y axis, perpendicular to the crystal's polar axis z. The fundamental beam [red beam in Fig. 1(a)] has a Gaussian distribution, and is incident on the 2D NPC. The wavefront of the SH (green beam) can only achieve a single-dimensional flat-top distribution in the x direction, as shown in Fig. 1(a). Here, we designed a 3D

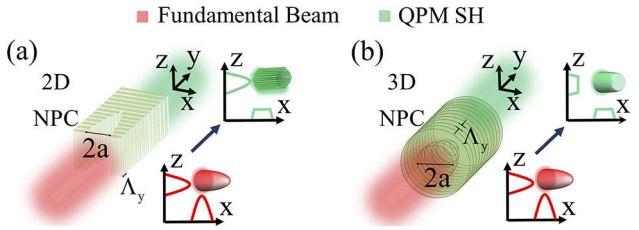

Fig. 1. Design principles of the 3D NPC. The intensity of the generated flat-top SH highly depends on the QPM mechanism. (a) When the fundamental beam is incident on the 2D NPC, the SH achieves flat-top distribution in one dimension. (b) Designed 3D conic NPC is able to add a dimension, enabling complete spatial wavefront shaping.

NPC with a conic contour to transform the Gaussian beam into a flat-top distribution [Fig. 1(b)]. After 3D NPC, the SH [green beam in Fig. 1(b)] can finally obtain a two-dimensional flat-top distribution, which makes the wavefront completely flat in the z–x plane.

We experimentally fabricated the 3D conic NPC inside a z-cut 5% MgO-doped $LiNbO_3$ crystal. Our fabrication process employed a representative femtosecond-laser writing system. The light source is a fs-pulsed laser (pulse width, 190 fs; repetition rate, 200 kHz) from a regenerative amplified Yb: KGW-based laser system with the wavelength of 1026 nm. A sample movement is manipulated by a high-precision displacement holder equipped with a PC-driven three-axis XYZ crossed-roller bearing positioning system, with a spatial resolution of 1 nm. The laser is focused with a 50× microscope objective (NA = 0.42), generating the light spot size of the processing focal plane about 1 μm. The femtosecond laser polarization is along the x direction of the crystal during processing. Maintaining the overall homogeneity of the structure is crucial for 3D NPC preparation. To compensate for focal spot distortion caused by aberrations and absorption loss, pulse energy needs to be adjusted with increasing depth. The pulse energy can be continuously adjusted through an attenuator consisting of a half-wave plate and a polarizing plate. The 20 layers are processed upward starting from a depth of 120 μm beneath the $+z$ surface of the crystal. The pulse energies of the top and bottom layers are 2.5 and 10 μJ, respectively. The scanning speed of the writing process is 100 $\mu m \cdot s^{-1}$.

After the laser processing, the 3D conic NPC and its x–y cross section are visualized by the Čerenkov-type SH confocal microscopy, as shown in Fig. 2. The units of the 3D conic NPC are displayed in Fig. 2(a) and Fig. 2(b) from different views. Based on QPM conditions, the period is $\Lambda_y = 6.3$ μm for the fundamental beam wavelength of 1030 nm. The duty cycle is 1/6.3. Each unit is a circle with an outer diameter of 100 μm in the x–z plane as shown in Fig. 2(b). Its inner diameter is calculated according to Eq. (1) and varies with the transmission distance. Figures 2(c)–2(f) display the characteristic end portions of different conic QPM gratings (truncated at a = 0, a = ±0.5ω, a = ±0.75ω, and a = ±0.8ω). Femtosecond laser pulse modification leads to the changes of the crystal's $\chi^{(2)}$ and refractive index. Obviously, a clear periodic structure with complete and homogeneous morphology is shown within the modified region.

Next, the Gaussian to flat-top beam shaping experiment is performed. To achieve a fundamental beam with a spot diameter of 100 μm, we employed a laser beam reduction system that

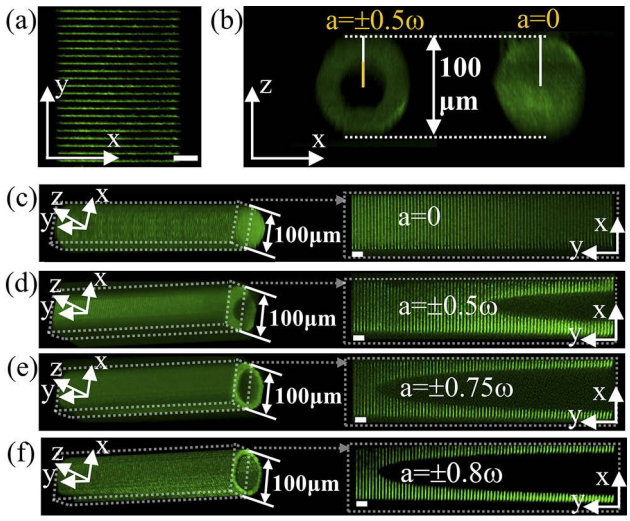

Fig. 2. Portion of beam shaping NPC, visualized by the Čerenkov-type SH confocal microscopy. The total length L_0 of the QPM grating is 630 μm. (a) Side view of the NPC units (the length of scale bars, 20 μm). (b) Front view of the NPC units. (c)–(f) 3D conic NPC at various truncation factors (the length of scale bars, 20 μm).

includes a concave lens (15 mm focal length) and a convex lens (750 mm focal length). The fundamental beam has the wavelength of 1030 nm, pulse duration of 270 fs and repetition rate of 100 kHz. The y axis of the sample is set to be along the propagation direction of the input light, and its z axis is set along the vertical direction. Image acquisition is performed using a CCD camera. The second harmonic emitted from the crystal is expanded by a 4× beam expander. The CCD collects data at a distance of 100 mm from the crystal emission end. The CCD is replaced with a powermeter when power measurements are required. The powermeter has a minimum resolution accuracy of 0.1 μW. Interference stray spots appear in the SH intensity distribution image captured by the CCD. These are primarily due to two factors: the existence of unremovable stains inside the CCD lens and the wavefront interference caused by laser transmission reflecting back and forth within each component, resulting in a highly divergent shadow distribution and interference ring. However, these have negligible effects on the data calculation and statistics of the subsequent results. In theory, there is no difference in the interaction length and conversion efficiency during propagation whether the fundamental wave is incident along the y axis or the $-y$ axis. However, a slight disparity in the refractive index distribution between the front and back ends of the crystal is observed during the experiment, leading to minor deviations in the experimental results for these two propagation modes. Nevertheless, these practical processing distinctions can be neglected. We measured and observed that the experimental results for both propagation modes are nearly identical. The pump light is incident independently on the structures of Figs. 2(c)–2(f).

Figure 3 depicts the SH beam intensity distribution at a pump beam power of 0.082 mW. As the truncation factor increases, the flat-topped region in the SH beam cross section enlarges. The normalized intensity along the horizontal pixel line [dashed white lines in Figs. 3(a)–3(d)] is presented in Fig. 4(a). Similarly, the normalized intensity along the vertical pixel line [solid white

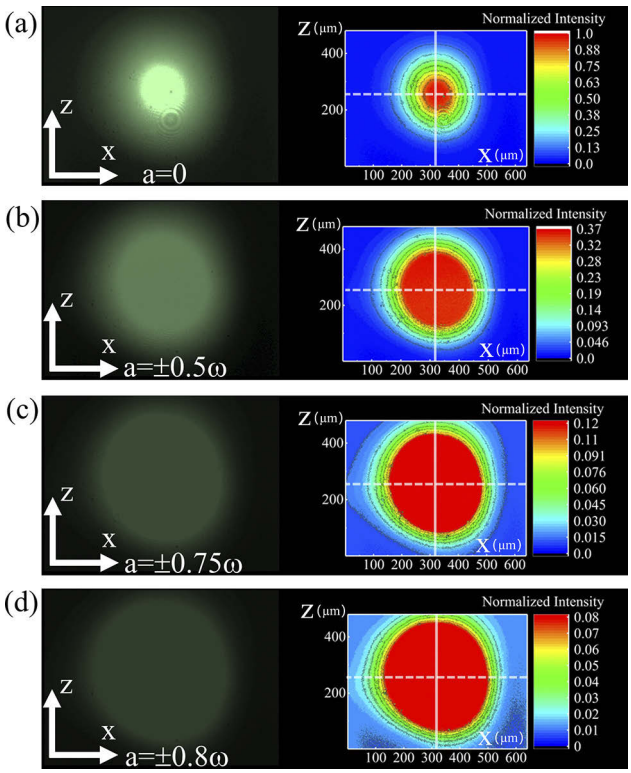

Fig. 3. SH beam's intensity distribution and normalized intensity contour distribution (a) Truncation factor of 0. (b) Truncation factor of ±0.5ω. (c) Truncation factor of ±0.75ω. (d) Truncation factor of ±0.8ω.

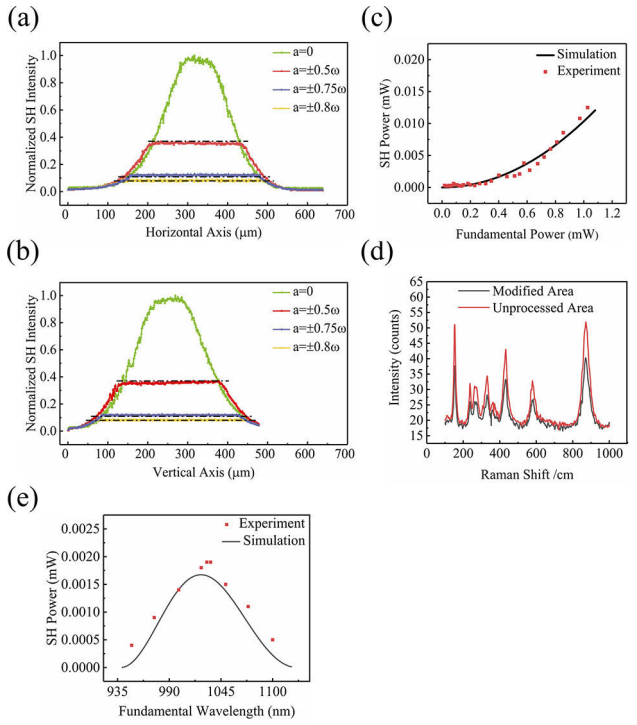

Fig. 4. (a),(b) Normalized intensity slices through the generated SH beams, obtained from a single line of pixels of the CCD camera at the spot center. Dashed black lines represent theoretical predictions for the flat portions of the truncated beams. (a) Along the x axis (corresponding to the dashed white lines in Fig. 3). (b) Along the z axis (corresponding to the solid white lines in Fig. 3). (c) Output SH powers after beam shaping by the NPC of truncation factor of ±0.5ω versus pump power at the QPM wavelength of 1030 nm. At a pump power of 1.027 mW, the output SH power reaches 0.0125 mW. (d) Micro-Raman signal of the processed area and the unprocessed area. (e) SH power dependence on the fundamental wavelength when the input power of the fundamental beam is 0.4 mW.

lines in Figs. 3(a)–3(d)] is shown in Fig. 4(b). The dashed black lines in Figs. 4(a) and 4(b) represent the theoretical predictions for the flat portions of the truncated beams. The beam shaping structures, with truncation factors of $a = \pm 0.5\omega$, $a = \pm 0.75\omega$, and $a = \pm 0.8\omega$, produce flat SH beams in two dimensions with normalized peak intensities of 0.363, 0.125, and 0.085 in the horizontal direction and 0.359, 0.121, and 0.081 in the vertical direction, respectively. These values are nearly identical to those reported in 1998 [11]. The experimentally measured SH intensities, obtained after shaping, closely match the corresponding theoretical values.

The flatness factor, according to ISO 13694 [28], is determined by dividing the average irradiance by the maximum irradiance, indicating how closely the actual beam resembles an ideal flat-top beam. Evaluating from Figs. 4(a) and 4(b), the flatness factors for the SH beam, with truncation factors of $a = \pm 0.5\omega$, $a = \pm 0.75\omega$, and $a = \pm 0.8\omega$, are 0.971, 0.933, and 0.948 in the horizontal direction and 0.966, 0.931, and 0.909 in the vertical direction, respectively. The SH beam's flatness factor is more closely related to the value of 1, indicating that the beam's flatness and homogenization are better.

Dependence of output power of the SH beam on the pump power is shown in Fig. 4(c). The effective nonlinearity is 0.223 pm/V. The simulated curve (calculated from Eq. (7) of Supplementary note 4 in Ref. [24]) agrees well with the experimental results. At a fundamental input power of 1.027 mW (peak power approximately 37 kW), the power conversion efficiency of the 3D NPC with truncation factor of $a = \pm 0.5\omega$ is about 1.22×10^{-2}. Given the low conversion efficiency, the small-signal approximation suffices for the solution. Additionally, taking into account the order of magnitude of the interaction length, we neglect the group velocity dispersion. Increasing the QPM length, upping the fundamental input energy, and adjusting the duty cycle can help to increase conversion efficiency [18]. The duty cycle can be adjusted by changing the move-step during the laser processing.

In our experiment, the conversion efficiency is affected by the slight change of the refractive index. Figure 4(d) displays the micro-Raman signal of the processed area and the unprocessed area. The Raman signal in the fabrication region noticeably weakens, indicating a significant decrease possibly due to a change of the physical structure [15]. The depletion ratio is 0.275 based on the Raman spectrum. By measuring the intensity of the central spot and the intensity of the nonzero level diffracted spot [29], we calculated that the change of the refractive index is approximately 8×10^{-3}. Figure 4(e) shows the simulated and measured relationship between the SH power and fundamental wave wavelength at an input power of 0.4 mW with the temperature 20°C [30].

In conclusion, we have experimentally achieved the nonlinear Gaussian to flat-top beam shaping through the 3D NPC with femtosecond laser modification. The measured profile flatness for the flat-top SH with various truncations exceeds 90% in

mutually perpendicular coordinates, with the best flatness reaching 97.1%. The precision of femtosecond pulse modification is currently limited to 1 micron, preventing us from achieving an ideal flat-top beam with a truncation value of 1. There are some aspects that need to be considered in the future. Further optimizations include improving the precision of femtosecond pulse modification, addressing non-uniformity resulting from finite-bandwidth femtosecond pulses, and mitigating the effects of group velocity mismatch between fundamental and second-harmonic pulses. Additionally, challenges such as diffraction, optical aberration during laser transmission, and limitations on the effective interaction distance for nonlinear processes need to be addressed. Our 3D NPC offers an extra dimension, which can simultaneously achieve nonlinear frequency conversion and full-wavefront shaping. This provides a convenient and practical way to generate nonlinear flat-top beams with two-dimensional distribution and has implications for the other nonlinear beams with special wavefront distributions, such as toroidal beams.

Funding. Strategic Priority Research Program of Chinese Academy of Sciences (XDA25040201); Taishan Scholar Program, Outstanding Youth Foundation of Shandong Province, China (tsqn202312207); Qingdao New Energy Shandong Laboratory Open Project (QNESL OP 202305).

Acknowledgment. We would like to acknowledge support from the Key Laboratory for Laser Plasmas (Ministry of Education).

Disclosures. The authors declare no conflicts of interest.

Data availability. Data underlying the results presented in this paper are not publicly available at this time but may be obtained from the authors upon reasonable request.

REFERENCES

1. N. Nishi, T. Jitsuno, K. Tsubakimoto, *et al.*, Opt. Rev. **7**, 216 (2000).
2. S. Sakata, S. Lee, H. Morita, *et al.*, Nat. Commun. **9**, 3937 (2018).
3. M. Bailly-Grandvaux, J. J. Santos, C. Bellei, *et al.*, Nat. Commun. **9**, 102 (2018).
4. S. Saghafi, K. Becker, F. Gori, *et al.*, J. Biophotonics **15**, e202100342 (2022).
5. C. Zhao, Y. Cai, X. Lu, *et al.*, Opt. Express **17**, 1753 (2009).
6. Y. Deng, X. Ji, H. Yu, *et al.*, Opt. Express **27**, 14585 (2019).
7. H. Ma, Z. Liu, X. Xu, *et al.*, Opt. Lett. **35**, 2973 (2010).
8. N. Yu and F. Capasso, Nat. Mater. **13**, 139 (2014).
9. V. Berger, Phys. Rev. Lett. **81**, 4136 (1998).
10. J. A. Armstrong, N. Bloembergen, J. Ducuing, *et al.*, Phys. Rev. **127**, 1918 (1962).
11. G. Imeshev, M. Proctor, and M. M. Fejer, Opt. Lett. **23**, 673 (1998).
12. N. G. R. Broderick, G. W. Ross, H. L. Offerhaus, *et al.*, Phys. Rev. Lett. **84**, 4345 (2000).
13. P. Xu, S. H. Ji, S. N. Zhu, *et al.*, Phys. Rev. Lett. **93**, 133904 (2004).
14. A. C. Busacca, C. L. Sones, R. W. Eason, *et al.*, Appl. Phys. Lett. **84**, 4430 (2004).
15. D. Wei, C. Wang, H. Wang, *et al.*, Nat. Photonics **12**, 596 (2018).
16. T. Xu, K. Switkowski, X. Chen, *et al.*, Nat. Photonics **12**, 591 (2018).
17. X. Xu, T. Wang, P. Chen, *et al.*, Nature **609**, 496 (2022).
18. X. Wang, Q. Cao, R. Wang, *et al.*, Appl. Phys. Lett. **121**, 6 (2022).
19. X. Wang, Q. Cao, R. Wang, *et al.*, Opt. Lett. **48**, 566 (2023).
20. S. Wang, S. Liu, D. Liu, *et al.*, Opt. Express **31**, 5843 (2023).
21. J. Imbrock, L. Wesemann, S. Kroesen, *et al.*, Optica **7**, 28 (2020).
22. Y. Chen, C. Yang, S. Liu, *et al.*, Adv. Photonics Res. **3**, 2100268 (2022).
23. S. Liu, K. Switkowski, C. Xu, *et al.*, Nat. Commun. **10**, 3208 (2019).
24. D. Wei, C. Wang, X. Xu, *et al.*, Nat. Commun. **10**, 4193 (2019).
25. C. Wang, P. Chen, D. Wei, *et al.*, ACS Photonics **10**, 456 (2023).
26. P. Chen, C. Wang, D. Wei, *et al.*, Light: Sci. Appl. **10**, 146 (2021).
27. S. Liu, L. M. Mazur, W. Krolikowski, *et al.*, Laser Photonics Rev. **14**, 2000224 (2020).
28. "Lasers and laser-related equipment: Test methods for laser beam power (energy) density distribution," ISO 13694-3 (2018).
29. J. Hua, F. Yu, Z. Tian, *et al.*, J. Laser Micro Nanoen. **12**, 207 (2017).
30. O. Gayer, Z. Sacks, E. Galun, *et al.*, Appl. Phys. B **91**, 343 (2008).